Nanoscale

PAPER

View Article Online
View Journal | View Issue

Cite this: *Nanoscale*, 2025, **17**, 25846

High-performance metal oxide nanoparticle materials synthesised using polar aprotic solvents for advanced supercapacitor applications

Muhammad Nasir Hussain,[a,b] Abid Inayat,[a] Syed Mujtaba Shah,[a] Mohammad Ihsun,[b] Ali Haider,[a] Syed Mustansar Abbas[c] and Stephen G. Hickey *[b]

We report on a newly developed, surfactant free and scalable methodology for the synthesis of spherical nanoparticles of nickel hydroxide [$Ni(OH)_2$] and nickel oxide (NiO), employing the polar, aprotic solvent, dimethylformamide (DMF), and evaluate their potential for electrochemical battery-type supercapacitor applications. The material synthesis methodology was extended to the hybrid nanomaterial nickel hydroxide-manganese dioxide [$Ni(OH)_2$–MnO_2] and, with the addition of SDBS, manganese dioxide (MnO_2) nanoparticles. The resulting nanostructured materials were comprehensively characterised by various structural, morphological, and thermal techniques. Of all electrode materials investigated in three-electrode configuration, surfactant free NiO and α-$Ni(OH)_2$–MnO_2 exhibit the highest specific capacities with values of 312.42 mAh g^{-1} and 348.61 mAh g^{-1} at a current density of 1 A g^{-1}, respectively. In symmetric devices, where surfactant free NiO and α-$Ni(OH)_2$–MnO_2 were employed as the active layers, specific capacities of 94.31 mAh g^{-1} and 139.43 mAh g^{-1} at a current density of 1 A g^{-1} and energy densities of 47.21 Wh kg^{-1} and 69.72 Wh kg^{-1} at a power density of 1 kW kg^{-1} respectively have been measured. The devices have a maximum capacity retention of 86.50% and 90.18% after 5000 charge–discharge cycles at 3 A g^{-1} demonstrating that they also possess high cycle stability. These results confirm the viability of the rational design methodology employed here for the surfactant free synthesis of electrode materials for deployment in energy storage applications.

Received 7th May 2025,
Accepted 11th October 2025

DOI: 10.1039/d5nr01871d

rsc.li/nanoscale

Introduction

Globally, there has been an increase in demand for appliances that can provide energy while on the move, much of which is due to the ever-expanding use of various portable devices as well as technological advances in areas such as hybrid electric vehicles. This, in turn, has resulted in an intensification in research efforts to develop the promising new electrode materials that are required for more efficient, lightweight energy storage and the methodologies that can supply them.[1–3] Among the most extensively investigated device types, and consequently the materials required for their fabrication, have been supercapacitors, (electrochemical double layer, pseudocapacitive and hybrid), due to their high-power densities, excellent reversibility, longer-life cycles and higher energy densities.[2–4] Additionally, supercapacitors have the advantage that they can provide a higher rate of energy discharge than the present generation of batteries. Pseudocapacitors are devices that do not purely rely on electrostatic processes, as in electrochemical double layer capacitors (EDLC), but also employ fast and reversible electrochemical processes (faradaic reactions) that involve near-surface charge transfer for energy storage. The mechanism by which energy is stored in pseudocapacitors therefore lies between that of EDLCs where the energy is stored in the double-layer, and batteries which primarily depend on faradaic electron transfer to metal centres mediated by the intercalation of ions such as Li^+ or Na^+. Current–voltage curve profiles can be used to differentiate the mode of charge storage and consequently distinguish which device type is in operation. Typically, EDLCs demonstrate potential-independent capacitance and current. By comparison, batteries display distinct oxidation and reduction peaks indicative of the metal centres involved in the charge storage. Additionally, in EDLCs, the discharge profiles of potential (E) *vs.* time (t) at constant current result in a linear plot while in batteries the E *vs.* t profile is non-linear with pla-

[a]*Department of Chemistry, Quaid-i-Azam University, Islamabad, 45320, Pakistan*
[b]*School of Chemistry and Biosciences, University of Bradford, BD7 1DP, UK. E-mail: S.Hickey1@bradford.ac.uk*
[c]*Nanoscience and Technology Department, National Centre for Physics, Islamabad, Pakistan*

teaus corresponding to the potential at which the oxidation and reduction of the metal centres occur. The *E vs. t* behaviour of pseudocapacitors lies between that of EDLCs and batteries. Typically, the capacitance and charge storage ability of supercapacitors is highly dependent on the electrode materials used in their manufacture and presently, one of the most promising types of electrode materials are nanostructured materials, due to their high surface to volume ratio and the fact that they provide relatively short path lengths for the transportation of electrons and ions.[1–5]

To date, a variety of electrode materials have been investigated for their supercapacitor properties, amongst which are carbon materials,[6] metal oxides/hydroxides[7–17] and conducting polymers.[18] Additionally, the combination of different materials to form composites or hybrid materials is predicted to bring advances with respect to enhancing the performance of supercapacitors. Recently, $Ni(OH)_2$ and MnO_2 based nanomaterials have been extensively employed in supercapacitor applications due to their relative abundance, low cost, high theoretical specific capacitance and their relatively low environmental impact.[19–30] $Ni(OH)_2$ has also been employed as a precursor in the synthesis of NiO nanostructures, and is a useful industrial material in its own right due to its valuable electronic, magnetic, and catalytic properties.[31] In recent years, numerous strategies have been applied for the fabrication of $Ni(OH)_2$ and MnO_2 nanostructures so that they possess desirable morphology, porosity, defect chemistry and crystal structures.[32–39] A major portion of that research has been focused towards the synthesis of $Ni(OH)_2$ and MnO_2 of various sizes, shapes and morphologies such as nanosheets,[40–42] nanorods,[38] nanobelts,[43,44] nanotubes,[39] hollow microspheres[32] and various nanocomposites.[45–47]

Traditionally, nanostructures have been synthesised by hydrothermal or solvothermal treatment at elevated temperatures and, in many cases, elevated pressures. Despite some success in the synthesis of metal oxide nanostructured materials using these methods, the design of an uncomplicated, easy to implement and more eco-friendly protocol still remains an important challenge to be realised. Ideally such a protocol would also assist in overcoming many of the issues associated with prolonged electric heating to achieve the high temperatures and increased pressures often required. Additionally, many of these methods require the presence of surface-active agents, such as long chained carboxylic acids, phosphonic acids or amines, which attach to the particle surface, impede charge transfer and need to be exchanged or removed if the nanomaterials are to be employed in electrochemical, electronic, or optoelectronic applications.

The synthesis of nanostructures in solvent media has attracted much attention because it provides an industrially viable and simple route to control the uniform size and shape of the resulting materials. Additionally, the use of polar, aprotic solvents has significant advantages over the use of polar, protic solvents in that polar, aprotic solvents tend to decrease the activation energy and lead to a successful completion of the reaction, whereas polar, protic solvents tend to increase the activation energy in syntheses where anionic species are present. This is due to the presence of strong hydrogen bonding between the anion and the polar, protic solvent, a process generally known as the solvation effect.[48] DMF has been reported to play an important role as a solvent medium that has a direct interaction with the reacting species that can induce the successful synthesis of high quality, mesoporous nanostructured materials.[49–52] Also, the use of polar aprotic solvents aid in stabilising reaction intermediates, can provide alternative mechanistic pathways and promote reactant solubility, all of which favourably affect reaction rates. The effects of DMF on the kinetics of nanomaterial synthesis are influenced by its unique properties such as high dielectric constant (36.71) and low viscosity (0.92 mPa s) which promote efficient solvation and diffusion of reactants. This can enhance mass transfer, allowing reactants to come into contact more readily, thereby accelerating reaction kinetics. The increased concentration of dissolved reactants can lead to faster nucleation rates. The enhanced solubility of reactants in DMF can lead to faster nucleation and growth rates of nanoparticles. The polar nature of DMF acts to stabilize reaction intermediates thus preventing agglomeration of the nanoparticles. On the other hand, due to its high boiling point, DMF can be used to accelerate reaction rates through increasing reactant mobility and consequently collision frequency. Furthermore, DMF is frequently used in the synthesis of metal nanoparticles, where it is employed as a reducing agent. Additionally, conventional sol–gel and hydrothermal methods often involve multiple steps, complex mixtures of surfactants, employ higher temperatures and require longer duration treatments. By contrast the method reported here enables the formation of uniform nanostructures under relatively mild conditions and with relatively shorter reaction times. Furthermore, unlike mechanochemical approaches, which can lead to particle agglomeration and limited morphology control, DMF as a medium provides a homogeneous reaction environment that promotes better dispersion and morphology regulation.

In this work we report on the synthesis of a range of oxidic materials for charge transfer applications; α-$Ni(OH)_2$, NiO, and α-$Ni(OH)_2$–MnO_2 hybrid nanostructures in DMF using a newly developed, solvothermal, synthetic protocol. The protocol allows for surfactant free syntheses, is easily implemented using standard laboratory glassware and is simple to scale-up. Additionally, we demonstrate the versatility of the procedure by extending it to the synthesis of a surfactant coated metal oxide nanomaterial (MnO_2) whose performance is compared to that of the surfactant free materials. To the authors knowledge this the first time that the use of DMF, both as a solvent medium as well as solubilising agent for the preparation of metal hydroxide/oxides nanoparticles, in which the synthetic procedure does not proceed by any reduction mechanism, is reported upon.[49] Subsequently, to test the hypothesis that this protocol is advantageous in fabricating materials with bare surfaces suitable for charge storage applications, the as-synthesized nanostructures were evaluated for their applicability

as electrode materials for pseudocapacitor devices. The exceptional capacitive performance of the porous NiO nanoparticles and α-$Ni(OH)_2$–MnO_2 hybrid composite are attributed to their surfactant free morphology, confirming the advantages of employing this procedure to prepare electrode materials for energy storage devices. The results have shown this newly developed synthetic protocol to be a powerful tool for the fabrication of a range of high quality, crystalline, nanostructured oxidic materials for electrochemical applications.

Experimental section

Materials

All chemicals were purchased from Sigma-Aldrich and used as received without further purification: nickel(II) sulphate heptahydrate, ($NiSO_4 \cdot 7H_2O$, ≥99.9%), sodium hydroxide (NaOH, ≥98.0%), dimethylformamide (DMF, ≥99.8%), manganese(II) nitrate tetrahydrate ($Mn(NO_3)_2 \cdot 4H_2O$, ≥97.0%), sodium dodecyl benzene sulphonate (SDBS, technical grade) and potassium permanganate ($KMnO_4$, ≥99.0%).

Synthesis of α-$Ni(OH)_2$ nanoparticles

For the synthesis of α-$Ni(OH)_2$ nanoparticles, a mixture of $NiSO_4 \cdot 7H_2O$ (2.75 g, 9.8 mmol) and NaOH (0.132 g, 3.3 mmol) in 40 mL DMF were degassed in a 50 mL, three necked, round-bottomed flask under vacuum and with vigorous stirring at 60 °C for 1 h. The temperature of the mixture was then maintained at 120 °C for 24 h. Subsequently, the reaction mixture was centrifuged at 6000 rpm for 5 minutes which resulted in the separation of a green paste-like precipitate and a clear supernatant, the latter of which was decanted off. The green paste was subsequently washed three times with deionised water and dried in an oven at 60 °C for 12 h which yielded a green crystalline powder, identified as α-$Ni(OH)_2$. This material was subsequently used as an intermediate for the synthesis of both the NiO and α-$Ni(OH)_2$–MnO_2 hybrid nanostructures.

Synthesis of NiO nanoparticles

Nanoparticles of NiO were obtained directly by annealing the as-synthesized α-$Ni(OH)_2$ in a furnace at 500 °C for 2 h.

Synthesis of α-$Ni(OH)_2$–MnO_2 hybrid nanostructures

In a typical synthesis of α-$Ni(OH)_2$–MnO_2 hybrid nanostructures, 50 mg of the above synthesized $Ni(OH)_2$ nanoparticles were placed in a 50 mL three necked, round-bottomed flask and dispersed in 30 mL of DMF. Then, 10 mL of 0.08 M $KMnO_4$, prepared in DMF, was added to the suspension and the mixture degassed under vacuum. The solution was kept under constant stirring for 3 h. The temperature of the mixed solution was then maintained at 150 °C for 5 h and subsequently allowed to cool down to room temperature naturally. The reaction mixture was centrifuged at 6000 rpm for 5 minutes, the precipitate washed three times with deionised water and dried at 60 °C for 6 h.

Synthesis of MnO_2 nanoparticles

In a typical synthesis of MnO_2 nanoparticles, $Mn(NO_3)_2 \cdot 4H_2O$ (0.2685 g, 1.07 mmol) and sodium dodecyl benzene sulfonate (SDBS, 0.3845 g, 1.1 mmol) were dissolved in 30 mL of DMF in a 50 mL three necked, round-bottomed flask. When the solution turned clear, 5 mL of 0.2 M $KMnO_4$ was added, and the mixture degassed under vacuum for 30 minutes at room temperature while continuously stirring. The temperature of the resulting solution was then maintained at 150 °C for 6 h and subsequently allowed to cool down naturally to room temperature. The reaction mixture was centrifuged at 6000 rpm for 5 minutes, the precipitate washed three times with deionised water and dried at 60 °C for 6 h. Here SDBS is used as a capping agent in the synthesis and, as MnO_2 can be synthesized in a variety of morphologies, to effectively control the resulting spherical geometry of the MnO_2 nanoparticles.[53] The synthesis of this material also allows for the comparative assessment of the performance of a surface coated *versus* a non-coated nanomaterial.

Physical characterization

The phase purity and structural analysis of the nanostructures was studied by P-XRD (Bruker advance AXS D8) analysis, Raman (Renishaw InVia instrument), and FTIR (PerkinElmer Frontier 100) spectroscopy. X-ray photoelectron spectroscopy (XPS) (Kratos Axis Super instrument) was used to measure the oxidation states of each element in the sample. The SEM images were collected on an FEI Quanta 400. TEM images were obtained using a Jeol Jem-1200 EX MKII. The thermal behaviour was analysed by thermogravimetric analysis (TGA, TA Instruments Q5000), and differential scanning calorimetry (DSC, TA Instruments Q2000), respectively. Electrochemical investigations were carried out on a Gamry electrochemical workstation (interface 1010E). The specific methods used for sample preparation and data collection are described in the SI.

Electrode preparation and evaluation of the electrochemical properties

All electrochemical investigations pertaining to the charge storage properties were carried out on a Gamry electrochemical workstation (interface 1010E), in three-electrode mode, with Ag/AgCl/3 M KCl and Pt foil serving as the reference and counter electrodes respectively. All values of the potential reported are with respect to the Ag/AgCl/3 M KCl reference electrode. All measurements were conducted using 2 M KOH solution as background electrolyte. The electrochemical performance of the as-fabricated electrodes was elucidated *via* cyclic voltammetry (CV), which was carried out at various scan rates (10 to 100 mV s^{-1}) in the potential range of −0.2 to +0.6 V, and galvanostatic charge–discharge (GCD) was performed in the potential range of 0 to +0.4 V with current densities ranging from 1 to 10 A g^{-1}. Additionally, electrochemical impedance spectroscopy (EIS) was undertaken in the frequency range of 0.1 Hz to 100 kHz employing an ac modulated potential amplitude of 5 mV. For the supercapacitance investigations

a slurry was prepared and coated onto a nickel foam substrate to provide a 1 × 1 cm^2 surface area as the working electrode. The slurry was prepared by mixing 80 wt% of active material, 10 wt% of conductive reagent (carbon black), and 10 wt% of binder (polyvinylidene fluoride, PVDF) in *N*-methyl-2-pyrrolidone (NMP) under magnetic stirring. The mixture was then stirred for 12 hours, after which the resulting mixture was coated onto a nickel foam substrate, that had previously been cleaned and activated, by drop casting the slurry and allowing it to dry at 70 °C in an oven overnight. The mass of the active material was estimated from the mass difference of the substrate before and after coating with the slurry which was approximately 1 mg. The fabrication process for the symmetric device followed the same steps as for the three-electrode system, with the exception that the nickel foam dimensions are 2 × 3 cm^2.

Eqn (1) was used to calculate the specific capacity from the GCD curves for all electrodes fabricated:[54,55]

$$C_{sc} = 2\frac{I \times \int V\mathrm{d}t}{m \times V} \quad (1)$$

where I is the discharge current (A), $\int V\mathrm{d}t$ the area under the discharge curve, m the mass of the active material (g) and C_{sc} the specific capacity (mAh g^{-1}). The energy density (E in Wh kg^{-1}) and power density (P in W kg^{-1}) of the fabricated electrode materials were calculated using eqn (2) and (3), respectively:

$$E = \frac{I \times \int V\mathrm{d}t}{m \times 3.6} \quad (2)$$

$$P = \frac{E \times 3600}{\Delta t} \quad (3)$$

Results and discussion

The phase purity of the as-synthesized nanostructured materials was determined by powder X-ray diffraction, as presented in Fig. 1A. The diffraction patterns A(a, b, c, d) represent the α-$Ni(OH)_2$ (monoclinic), NiO (cubic), MnO_2 (tetragonal), and α-$Ni(OH)_2$–MnO_2 hybrid nanostructures, respectively. All peaks match well with the corresponding JCPDS entries for α-$Ni(OH)_2$ (no. 41-1424), NiO (no. 73-1523), and MnO_2 (no. 44-0141), with no additional peaks appearing in the profiles indicating that the materials are of single-phase. The peaks in the hybrid nanostructures are indicated using an asterisk (*) for α-$Ni(OH)_2$ and for MnO_2 using a hash (#). The average crystallite sizes, as calculated using Debye-Scherrer analysis, are presented in the SI. The structural properties of the as-synthesised nanostructures were additionally analysed by Raman spectroscopy (Fig. 1B). The α-$Ni(OH)_2$ nanostructure Raman active vibration modes appeared at 478 cm^{-1}, 611 cm^{-1}, and 998 cm^{-1} which can be assigned to the E_g(T), A_{1g}(T), and two order phonon modes respectively, as shown in profile B(a). For NiO, the Raman bands are assigned as a one longitudinal optical (LO) phonon (503 cm^{-1}), a two LO phonon (994 cm^{-1}) mode, and the peak at 1531 cm^{-1} arises due to two-magnon (2M) scattering as in profile B(b). Also, MnO_2 shows one band at 650 cm^{-1} due to symmetric stretching of the Mn–O lattice, presented in profile B(c). The α-$Ni(OH)_2$–MnO_2 hybrid nanostructures, profile B(d), exhibit two peaks, one at 515 cm^{-1} attributed to the stretching vibration of Ni–O and the other at 630 cm^{-1} to symmetric stretching of Mn–O lattice. The FTIR spectra supports these observations and are presented in Fig. S1.

The chemical state of the as-prepared α-$Ni(OH)_2$–MnO_2 hybrid material was investigated by X-ray photoelectron spec-

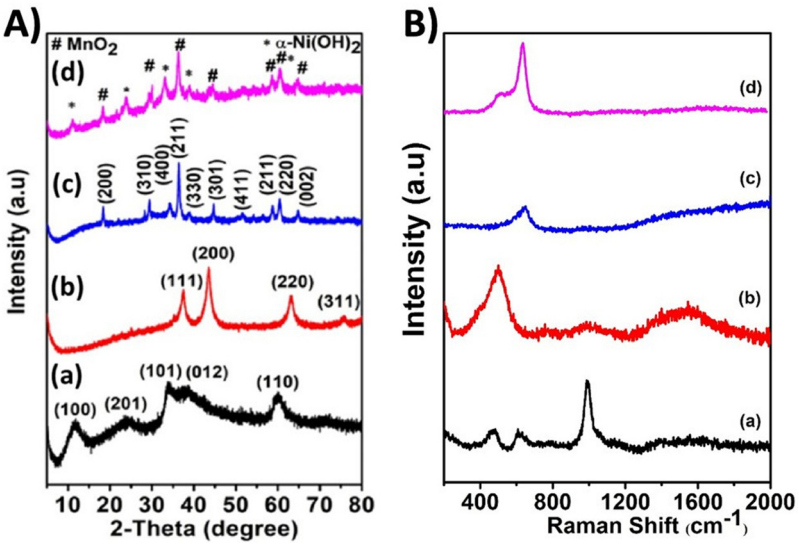

Fig. 1 (A) P-XRD diffractograms and (B) Raman spectra of (a) α-$Ni(OH)_2$ nanoparticles, (b) NiO nanoparticles, (c) MnO_2 nanoparticles and (d) α-$Ni(OH)_2$–MnO_2 hybrid nanomaterial.

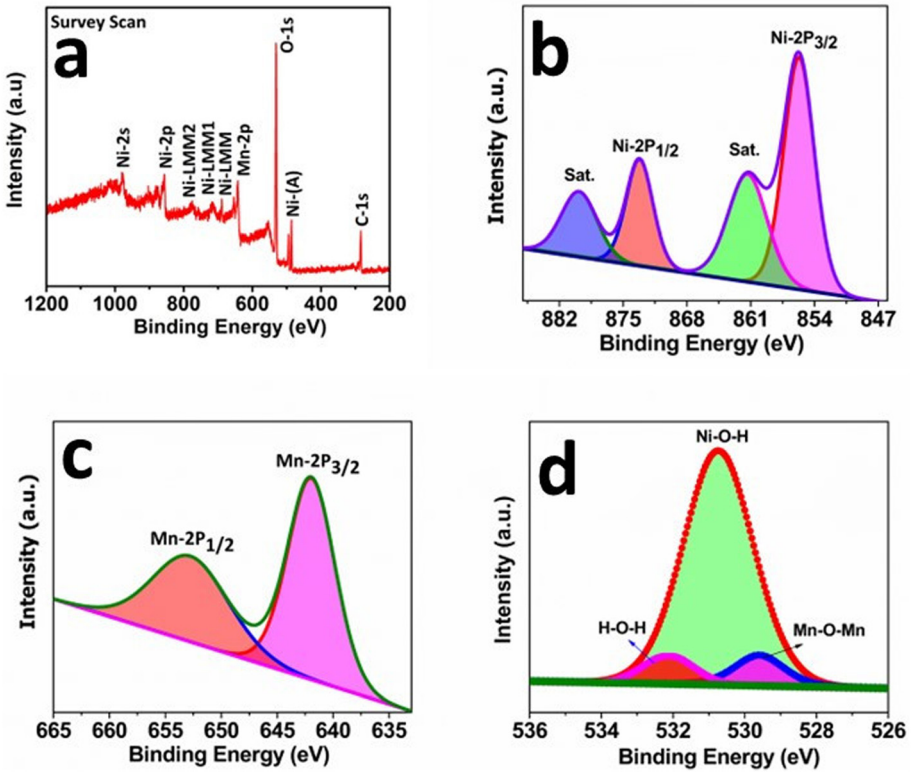

Fig. 2 XPS spectra of α-$Ni(OH)_2$–MnO_2 hybrid, (a) survey scan, (b) Ni-2p, (c) Mn-1p, (d) O-1s.

troscopy (XPS). The survey spectrum of α-$Ni(OH)_2$–MnO_2 confirms the presence of Ni, Mn, and O as depicted in Fig. 2(a). The presence of the Ni 2p core-level is distinguished by two spin–orbit peaks at 872.2 eV (Ni $2p_{1/2}$) and 854.3 eV (Ni $2p_{3/2}$), as well as their two strong satellite peaks, which indicate the existence of the Ni^{2+} state in the hybrid as shown in Fig. 2(b).[56,57] The satellite peaks of the Ni $2p_{3/2}$ and Ni $2p_{1/2}$ peaks are located at 861.4 eV and 879 eV, respectively. Importantly, Ni $2p_{1/2}$ and Ni $2p_{3/2}$ are clearly distinguished at a separation of 17.9 eV. The two peaks centred at 653.1 eV (Mn $2p_{1/2}$) and 642.3 eV (Mn $2p_{3/2}$) in the Mn 2p XPS spectra show that in the hybrid materials the manganese exists in the Mn^{4+} oxidation state, as presented in Fig. 2(c).[58] The deconvoluted O 1s spectrum contains three sub-peaks located at 530.7, 531.6, and 532.8 eV which can be assigned to the Mn–O–Mn, Ni–O–H, and H_2O, respectively, see Fig. 2(d).[59]

The surface morphology of the as-prepared nanostructures was imaged by scanning electron microscopy (SEM) as shown in the top row of Fig. 3. α-$Ni(OH)_2$ consists of a large quantity of smooth and uniformly shaped nanoparticles Fig. 3(a) with the diameters of the individual objects being in the range of 40 to 60 nm. The NiO nanoparticles Fig. 3(b) are approximately spherical in shape and of different sizes, with typical diameters in the range of 50 nm to 60 nm. Also, the morphology of the particles observed in the image suggests that most of the particles are agglomerates of smaller individual moieties. The MnO_2 nanoparticles were also identified as spherical in shape Fig. 3(c), with diameters of about 50 nm. The existence of these spherical aggregates suggests a homogeneous nucleation process of MnO_2 under the conditions employed.[60] In addition, the α-$Ni(OH)_2$–MnO_2 hybrid nanostructures seen in Fig. 3(d) show that the α-$Ni(OH)_2$ nanoparticles are uniformly decorated on the surface of the MnO_2 nanoparticles in the hybrid material. Hence, a degree of control over the morphology of the as-synthesised nanostructures could be exercised and subsequently optimised by applying this additional step in the solvothermal treatment. In the middle row of Fig. 3 the elemental mapping of the α-$Ni(OH)_2$–MnO_2 nanostructures is presented. Fig. 3(e) is a low magnification overview of the as-synthesised material showing the homogeneous distribution of manganese, nickel and oxygen, testifying to the uniformity of the distribution of each element in the sample. The broader Mn distribution arises from its stronger X-ray emission compared to that of the weaker O signal, which is limited by low atomic number and higher absorption. The thermal behaviour of the nanostructures was analysed through TGA and DSC and are presented in Fig. S2.

High magnification TEM images of the as-prepared nanostructures Fig. 3(f) reveal that α-$Ni(OH)_2$ is composed of well distributed spherical nanoparticles having diameters in the range of 10 to 15 nm with a consistent size uniformity of the nanoparticles evidenced from the image. A typical TEM image of the porous NiO nanoparticles obtained by thermal decomposition of α-$Ni(OH)_2$ at 500 °C are presented in Fig. 3(g). A difference in the diameter of the nanoparticles compared to that of the α-$Ni(OH)_2$ precursor can be observed

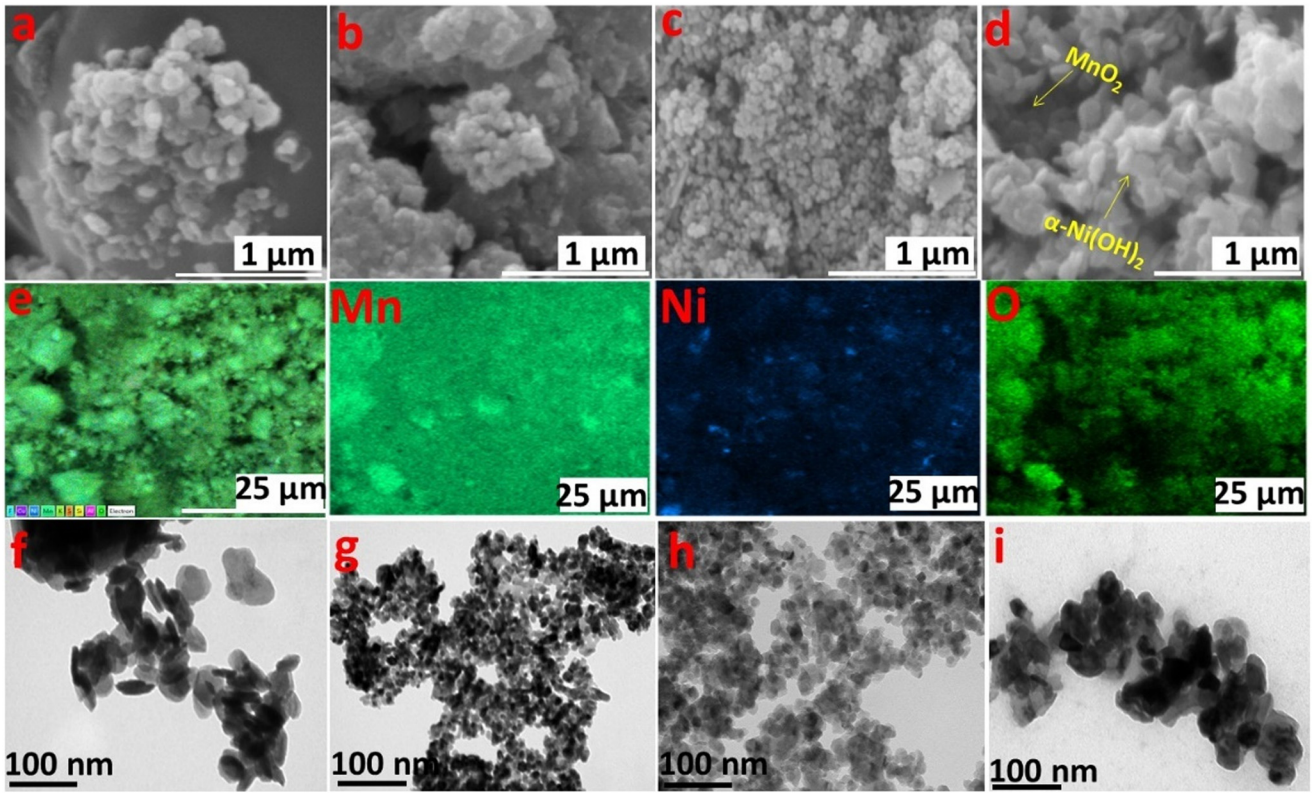

Fig. 3 Top row: SEM images of (a) α-$Ni(OH)_2$, (b) NiO, (c) MnO_2, and (d) α-$Ni(OH)_2$–MnO_2 hybrid. Middle row: elemental mapping images of (e) α-$Ni(OH)_2$–MnO_2 hybrid nanomaterials followed by images of the Mn, Ni and O distributions. Bottom row: TEM images of (f) α-$Ni(OH)_2$, (g) NiO, (h) MnO_2, (i) α-$Ni(OH)_2$–MnO_2 hybrid nanomaterials.

and the structures appear to exhibit a greater degree of agglomeration after calcination. Additionally, the morphology present in the $Ni(OH)_2$ material was not perfectly retained after thermal decomposition to NiO and it should be highlighted that many voids can be clearly seen, indicating the extended structures formed by the NiO nanoparticles are porous. Furthermore, the MnO_2 material demonstrates spherical morphology Fig. 3(h) and it can also be observed from the image of the α-$Ni(OH)_2$–MnO_2 hybrid nanostructures Fig. 3(i) that both the α-$Ni(OH)_2$ and MnO_2 nanoparticles are enlarged with respect to the size of their starting materials. The hybrid hierarchical aggregates consist of ultrafine MnO_2 nanoparticles interconnected with particles of α-$Ni(OH)_2$.

Electrochemical measurements in aqueous electrolytes

All electrochemical studies of the materials were carried out in various aqueous electrolytes presented in Fig. S3. Further, comprehensive investigations were undertaken using 2 M KOH as background electrolyte. The cyclic voltammograms (CV) of α-$Ni(OH)_2$ and NiO, Fig. 4(a and b), exhibit a typical battery-type behaviour with two broad redox peaks. Both anodic and cathodic peaks shift to higher and lower potential values respectively as the scan rate increases, suggesting that the redox reactions are controlled by the ion diffusion process which results from electrode polarization. Furthermore, increasing the scan rate leads to a gradual increase in the peak current, implying the presence of both ion and electron transfer in the electrode.[61] The profile of the curves remains unaltered with the increasing scan rate indicating excellent electrochemical stability of the active material. Moreover, the oxidation and reduction peaks of the NiO electrode remain almost symmetrical over the scan range of 10 to 100 mV s^{-1}, demonstrating strong reversibility of the redox reactions occurring at the electrode surface. There exists an inverse relationship between the specific capacity and scan rate which is as a consequence of the electrolyte ions having sufficient time to permeate into the electrode at lower scan rates, leading to full utilisation of the electroactive material. By contrast, at higher scan rates, the redox reactions only have time to occur at the outer surface, resulting in a decrease in the specific capacitance. The peaks present in the CV profile correspond to the surface oxidation/reduction reactions represented by eqn (4) and (5), the oxidation peak being due to the conversion of α-$Ni(OH)_2$/NiO to NiOOH and the reduction peak due to the reverse reaction.

$$Ni(OH)_2 + OH^- \Leftrightarrow NiOOH + H_2O + e^- \quad (4)$$

$$NiO + OH^- \Leftrightarrow NiOOH + e^- \quad (5)$$

Additionally, the NiO nanomaterial exhibits more promising electrochemical properties as a supercapacitor electrode material compared with α-$Ni(OH)_2$ due to its fast electron/ion

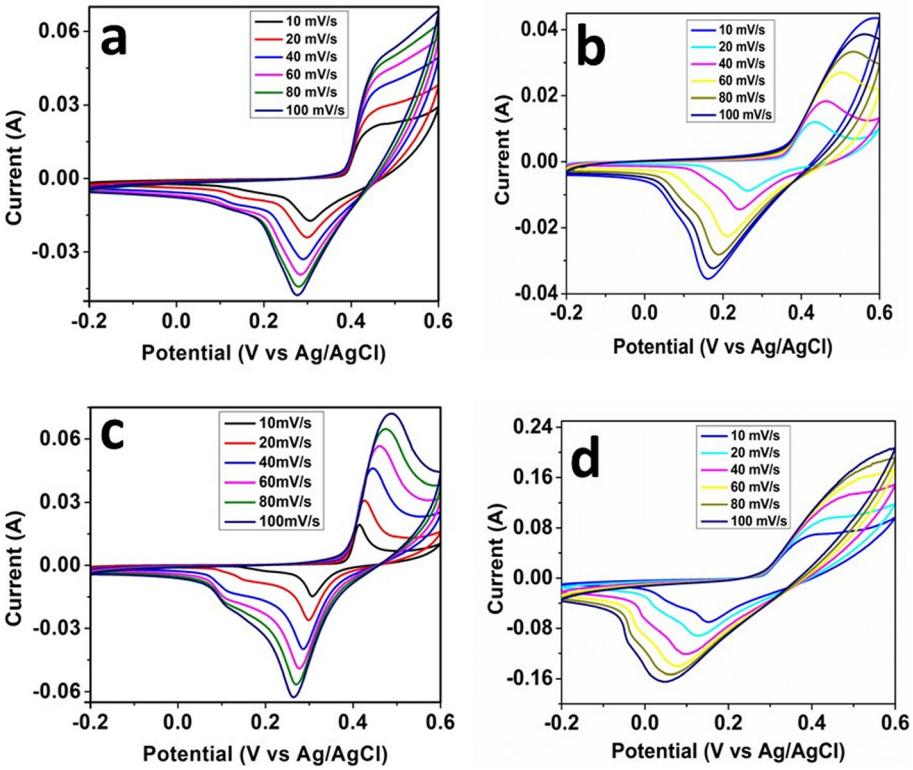

Fig. 4 CV profiles recorded at different scan rates in 2 M KOH of (a) α-$Ni(OH)_2$, (b) NiO, (c) MnO_2, and (d) α-$Ni(OH)_2$–MnO_2 hybrid nanomaterials.

diffusion rate during the faradaic reactions which is facilitated by the porous morphology[62,63] that results from this synthetic protocol and which enhances the feasibility for the material to be used in electrochemical applications. Evidence for this porosity was presented earlier in the TEM image of the NiO nanomaterial obtained by the thermal decomposition of the α-$Ni(OH)_2$ Fig. 3(g), where a closed interconnected network type structure could be observed. As a result of the porous nature of the nanostructure, ion diffusion is facilitated and consequently provides a more effective matrix for energy storage.[64] The presence of the larger pores allows for faster electrolyte ion transportation, while nanoscale sized undulations in the surface efficiently increase the available surface area upon which the redox reactions can occur.[65] This results in a material possessing a high degree of electrochemical performance in a structure that allows for a high storage capacity.

As can be seen from the CV's of the MnO_2 nanoparticles and α-$Ni(OH)_2$–MnO_2 hybrid under the same conditions (Fig. 4(c and d)), both materials also exhibit oxidation and reduction peaks, with the anodic peak for MnO_2 and α-$Ni(OH)_2$–MnO_2 occurring at +0.41 V and +0.39 V, and the cathodic peaks occurring at +0.30 V and +0.16 V respectively, at a scan rate 10 mV s^{-1}. As can be observed from Fig. 4(d), the integral area of the CV curve for the hybrid material is greater than that of MnO_2 nanoparticles, indicating that the hybrid material is capable of providing a higher specific capacity when evaluated for charge–discharge analysis. Typically, charge-storage in aqueous alkaline electrolyte proceeds by surface adsorption and desorption of ions from the electrolyte and the insertion of a proton from water. The general reaction for the pseudocapacitive processes of MnO_2 in aqueous solution may be represented for the general case by eqn (6) and, for the specific use of KOH as electrolyte, eqn (7).

$$MnO_2 + M^+ + e^- \Leftrightarrow MnOOM \quad (6)$$

$$MnO_2 + K^+ + e^- \Leftrightarrow MnOOK \quad (7)$$

where M^+ represents the metal ion in solution. Again, the CV profiles exhibit symmetric behaviour of the positive and negative sweeps at all scan rates, due to the fast reversible redox processes caused by the OH^- ions in the electrolyte system which also assists in improving the capacitive performance of the MnO_2 nanoparticle electrodes.

The high specific capacity of the hybrid material reported in this study is likely due to the synergistic effect between the MnO_2 and α-$Ni(OH)_2$ nanoparticles. As can be observed from the TEM image in Fig. 3(i), the α-$Ni(OH)_2$ nanoparticles are relatively evenly distributed on the surface of the MnO_2 nanoparticles, resulting in a high surface area which provides more active sites for the adsorption of electrolyte ions. Such a situation can improve electrochemical kinetics and ultimately lead to an enhancement of the specific capacity and improved supercapacitive performance.

Fig. 5(a and b) presents the galvanostatic charge–discharge (GCD) profiles of the as-prepared α-$Ni(OH)_2$ and NiO nanoparticles at various current densities, ranging from 1 to 10 A

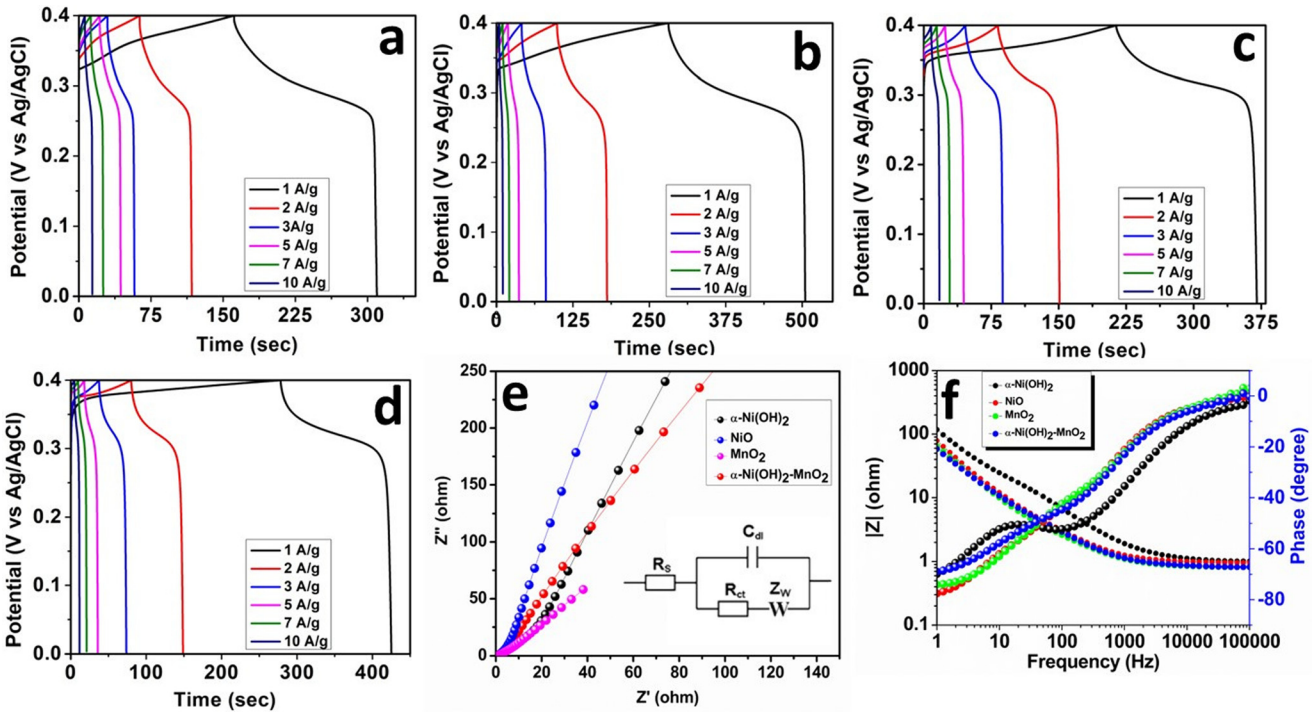

Fig. 5 GCD profiles of (a) α-$Ni(OH)_2$ nanoparticles, (b) NiO nanoparticles, (c) MnO_2 nanoparticles and (d) α-$Ni(OH)_2$–MnO_2 hybrid. Nyquist plots (e) and Bode plots (f) for all four materials.

g^{-1} over a potential window of 0 to +0.4 V, in aqueous 2 M KOH electrolyte solution. The non-linear discharge curves reflect the battery-type characteristics of the α-$Ni(OH)_2$ and NiO which is in agreement with the CV measurements.[64] NiO nanoparticles display the higher specific capacity of the two materials of up to 312.42 mAh g^{-1} at 1 A g^{-1}. At an even higher current density (10 A g^{-1}), an appreciable specific capacity of 241.12 mAh g^{-1} is still achieved. While the charge-storage behaviour is primarily as a result of the battery-type nature of the materials, through the redox reactions (Ni^{2+}/Ni^{3+}) that take place at the electrode–electrolyte interface, the specific capacity of the NiO nanomaterials is most likely enhanced by their distinctive morphology and high porosity. Electrolyte ions are expected to be readily absorbed by this type of structure, creating a region that can store OH^- ions for the redox reactions. As a result, the interaction between the electrode and electrolyte is increased and consequently the diffusion lengths are reduced, resulting in an acceleration in charge–discharge processes.[66,67]

Fig. 5(c and d) presents the GCD analysis at different current densities for the MnO_2 and α-$Ni(OH)_2$–MnO_2 hybrid materials under the same conditions. As previously observed, the non-linear slope of the curves is indicative of the redox active behaviour of the materials which again are in agreement with the CV curves. However, even at high current densities (*e.g.*, 10 A g^{-1}), the curves show that the redox reactions are reversible and symmetric in nature, demonstrating the high-performance rate of both these electrodes. In comparison to pure MnO_2 nanoparticles, which have a specific capacity of 104.41 mAh g^{-1}, the α-$Ni(OH)_2$–MnO_2 hybrid achieved an even higher value of 348.61 mAh g^{-1} revealing that the hybrid material has an increased performance over the pure MnO_2 nanoparticles. Moreover, it has been observed that MnO_2 nanoparticles can enable facile redox reactions and provide shorter diffusion lengths for electrons and ions.[21] This study reveals that the combination of both materials produces a synergistic effect that provides potential competitive benefits to α-$Ni(OH)_2$–MnO_2 hybrid-based supercapacitors. As at higher current densities oxygen evolution reactions can take place in aqueous electrolyte during the charging process, which impacts the GCD results,[68] different potential windows for the CV and GCD investigations were chosen.

In Fig. 5(e) electrochemical impedance spectroscopy (EIS) profiles of the nanostructures in the frequency range 0.01 Hz to 100 kHz at open circuit potential and under a superimposed ac potential amplitude of 5 mV are presented with the corresponding equivalent circuit model. Nyquist plots of all the materials display straight line behaviour in the lower frequency range due to their capacitive nature and a depressed arc in the high frequency region that is associated with the charge transfer resistance of the redox reaction occurring at the electrode–electrolyte interface, and which is increased due to the porous structure of the electrodes.[69] The bulk resistance is represented by the intercept with the real axis, and a shift to lower values indicates an increase in the bulk conductivity of the electrode. Here, NiO and α-$Ni(OH)_2$–MnO_2 electrodes exhibit minimum charge-transfer and series resistance in the high-frequency region, implying that both materials have a higher con-

ductivity and therefore more facile charge-transfer. Bode plots of all fabricated electrodes are presented in Fig. 5(f). The high frequency phase angles lie in the range of −70° to −77° which is quite close to −90°, demonstrating the near-ideal capacitive nature of the materials. The specific capacity values, as estimated from GCD curves, are summarized in Table 1.

The total capacity, arising from the quantitative contribution from the surface and diffusion capacities, of the electrodes can be estimated using eqn (8).

$$i(\mathrm{V}) = k_1 v + k_2 v^{1/2} \quad (8)$$

where $k_1 v$ accounts for the current contribution from the surface capacity and $k_2 v^{1/2}$ diffusion phenomenon, that is the intercalation/de-intercalation of the ions. Values of k_1 and k_2 may be obtained from a plot of $i(\mathrm{V})/v^{1/2}$ *vs.* $v^{1/2}$ at fixed potentials and various scan rates from CV curves (Fig. 6(a and c)).

Table 1 Specific capacity values of α-$Ni(OH)_2$ nanoparticles, NiO nanoparticles, MnO_2 nanoparticles and α-$Ni(OH)_2$–MnO_2 hybrid as calculated from GCD in mAh g^{-1}

Current density (A g^{-1})	1	2	3	5	7	10
α-$Ni(OH)_2$	136.21	102.45	81.67	58.41	42.87	27.31
NiO	312.42	301.11	285.83	280.56	263.27	241.12
MnO_2	104.41	82.64	63.31	55.73	42.77	33.43
α-$Ni(OH)_2$–MnO_2	348.61	348.43	321.16	282.52	272.22	244.34

The values of k_1 and k_2 determined for NiO are 0.71 A s V^{-1} and 20.77 A $s^{1/2}$ $V^{-1/2}$, whereas for α-$Ni(OH)_2$–MnO_2 the values are 0.52 A s V^{-1} and 9.38 A $s^{1/2}$ $V^{-1/2}$ respectively.

Fig. 6(b and d) shows the overall percentage capacity contribution from two different energy storage mechanisms at various scan rates. For NiO, at 10 mV s^{-1} the percentage contribution of the diffusion-controlled capacity (90%) is higher than that of the surface capacity (10%) with α-$Ni(OH)_2$–MnO_2 electrodes exhibiting a diffusion-controlled capacity contribution of 85% and 15% surface capacity. This high diffusion capacity contribution can be accounted for by the fact that at slow scan rates the electrolyte ions have more time to diffuse into the inner surface of the network. By contrast, the relative diffusion capacity contribution decreases at higher scan rates where it is expected that the contribution from surface processes become more prominent. The specific capacity contributions of surface and diffusion-controlled processes for α-$Ni(OH)_2$ and MnO_2 nanoparticles are provided in Fig. S4 within SI.

Electrochemical investigations in symmetric devices

All nanomaterials were subsequently tested within symmetric devices, in two electrode mode using Whatman filter paper as a separator. CV analysis was conducted for all devices in the potential window of 0 to 1 V, see Fig. S5. Interestingly, the CV profiles exhibited a rectangular shape at higher scan rates suggesting the kinetic reversibility of the symmetric devices. GCD analysis was conducted within the same potential

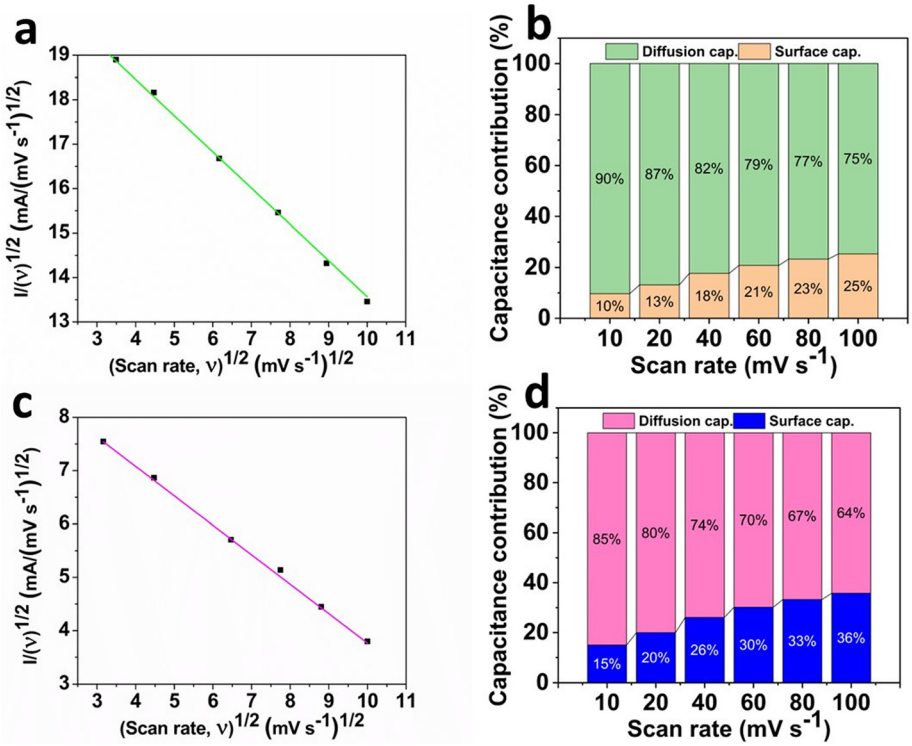

Fig. 6 Quantitative capacitive analysis of NiO nanoparticles and α-$Ni(OH)_2$–MnO_2 hybrid material, (a, c) plots of $(i/v^{1/2})$ *vs.* $(v^{1/2})$, (b, d) contribution of surface and diffusion capacities at various scan rate.

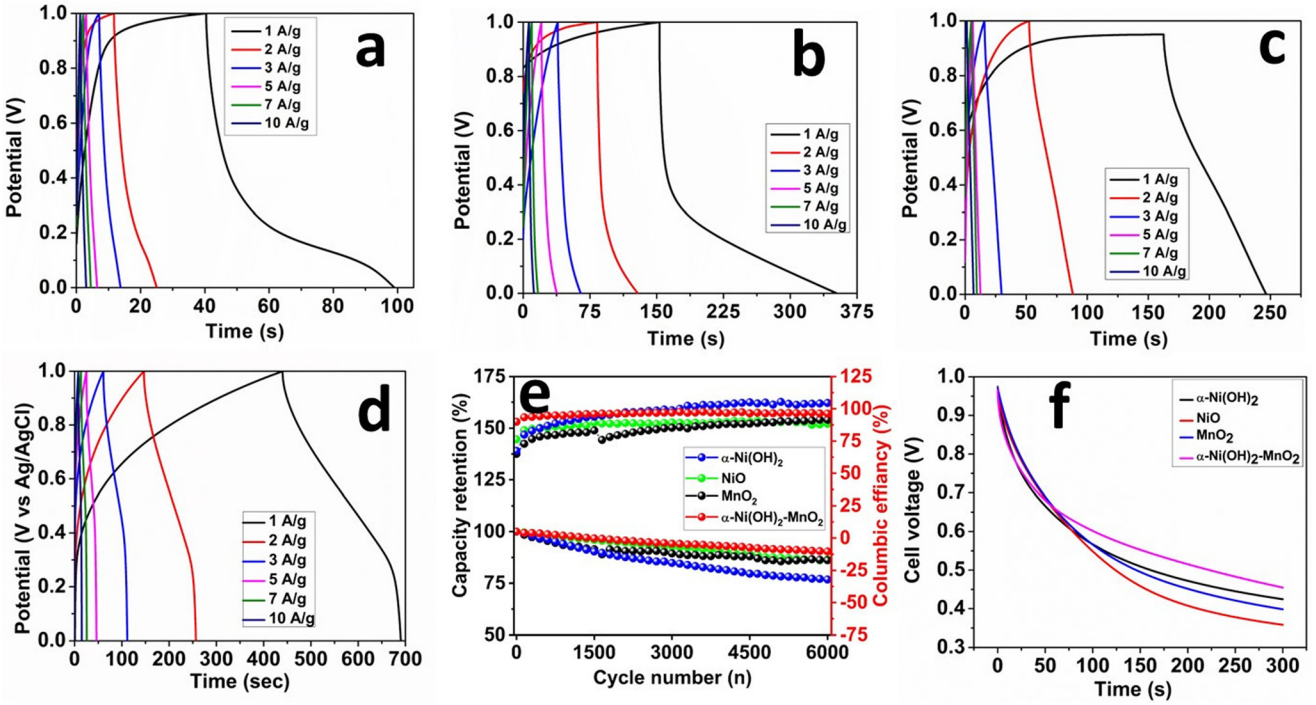

Fig. 7 GCD analysis of symmetric devices (a) α-$Ni(OH)_2$ nanoparticles, (b) NiO nanoparticles, (c) MnO_2 nanoparticles, (d) α-$Ni(OH)_2$–MnO_2 hybrid, (e) Cyclic stability and coulombic efficiency and (f) self-discharge curves.

window at current densities of 1 to 10 A g^{-1}, the findings of which are presented in Fig. 7(a–d). From the GCD curves, it is clear that the time required for charging and discharging symmetric devices is higher for lower current densities and lower for higher current densities. This occurs as at higher current densities the ions of the electrolytes are not being utilized over the total available area of the electroactive sites of the electrode while at lower current densities the electrolyte ions have sufficient time in which to diffuse into the bulk of the network. A sudden voltage drop (IR drop) was observed to occur during the crossover from the charge to discharge cycles due to the combined ohmic resistance of the electrode, electrolyte, and electrical contact resistance of the devices. The specific capacity values calculated for NiO, and α-$Ni(OH)_2$–MnO_2 are 94.31 mAh g^{-1} and 139.43 mAh g^{-1} at 1 A g^{-1}, respectively. The capacity retention as a function of the cycle number is presented in Fig. 7(e). The devices were tested over 5000 cycles and showed a capacity retention of 76.82, 86.50, 86.15 and 90.18% for all symmetric devices, indicating their excellent stability. The coulombic efficiency was determined from the ratio of the discharge to the charge time for every cycle of the GCD analysis presented. The coulombic efficiency values evaluated were 101.15, 89.55, 92.88, and 97.91% for all the devices. The comparative self-discharge potential profiles of the α-$Ni(OH)_2$, NiO, MnO_2 and α-$Ni(OH)_2$–MnO_2 electrodes initially charged at 1.0 V are presented in Fig. 7(f). From the discharge profile it can be seen that the α-$Ni(OH)_2$–MnO_2 has the slowest discharge rate while the NiO has the quickest. The NiO curve reaches a constant value of 0.36 V after a comparatively long discharge time. Nyquist plots, recorded in three-electrode configuration, showed a similar behaviour as can be seen from Fig. S6. The devices fabricated using NiO and α-$Ni(OH)_2$–MnO_2 possess the highest energy densities of 47.21 Wh kg^{-1} and 69.72 Wh kg^{-1} at power densities of 1 kW kg^{-1} respectively, which equates to a current density of 1 A g^{-1}, demonstrating the high-rate capability of the materials. It should be noted that the energy density values reported here are calculated based on the mass of the active material of a single electrode and not the total mass of the device. The performance of the NiO and α-$Ni(OH)_2$–MnO_2 based symmetric devices clearly demonstrate a wide potential window even at higher energy densities. Furthermore, while operating at 1 V in 2 M KOH electrolyte, no gas evolution could be observed, with the capacitance originating from the reversible faradaic redox processes associated with $Ni(OH)_2$, NiO, MnO_2, and α-$Ni(OH)_2$–MnO_2 hybrid. Table 2 highlights the comparative performances of the materials presented in this study with those reported in the recent literature.

In addition, post-electrochemical investigations were carried out on the as-fabricated electrodes (Fig. 8). P-XRD was conducted on various samples, however, only peaks associated with the Ni foam could be observed, most likely due to the much greater abundance of the Ni foam relative to the electroactive materials as seen in Fig. 8(a). The XPS profiles (Fig. 8(b–d)) confirm that no changes in their oxidation state have occurred. The potassium K-2p peaks appear in the XPS spectrum due to the presence of the KOH (Fig. S7). FE-SEM images for all of the electrodes fabricated were recorded after they had

Table 2 Overview of recently reported performance parameters for $Ni(OH)_2$, NiO, MnO_2 and $Ni(OH)_2$–MnO_2 from literature

Material	Synthesis conditions (temp., time)	Morphology	Specific capacitance ($F\ g^{-1}$)	Device config.	Cycle stability (%)	Eco-friendliness	Ref.
$Ni(OH)_2$	Hydrothermal (170 °C, 12 h)	3D flake	67	Symmetric	94	Moderate (aqueous system)	70
$Ni(OH)_2$	Hydrothermal (120 °C, 12 h)	Nanowires	95.6	Symmetric	80.4	Moderate (aqueous system)	71
NiO	Green synthesis (400 °C, 2 h)	Nanoparticles	239	Symmetric	89	Moderate (aqueous system)	72
NiO	Hydrothermal (120 °C, 2 h)	Flake	53	Symmetric	104	Moderate (aqueous system)	73
MnO_2	Microwave (100 °C, 2 h)	Nanosheets	218	Symmetric	78.6	High (non-aqueous system)	74
MnO_2	Hydrothermal (160 °C, 8 h)	Nanorods	56.13	Symmetric	79	Moderate (aqueous system)	75
Ni $(OH)_2$@MnO_2	Hydrothermal (180 °C, 16 h)	Core–shell	166.2	Asymmetric	101.4	Moderate (aqueous system)	76

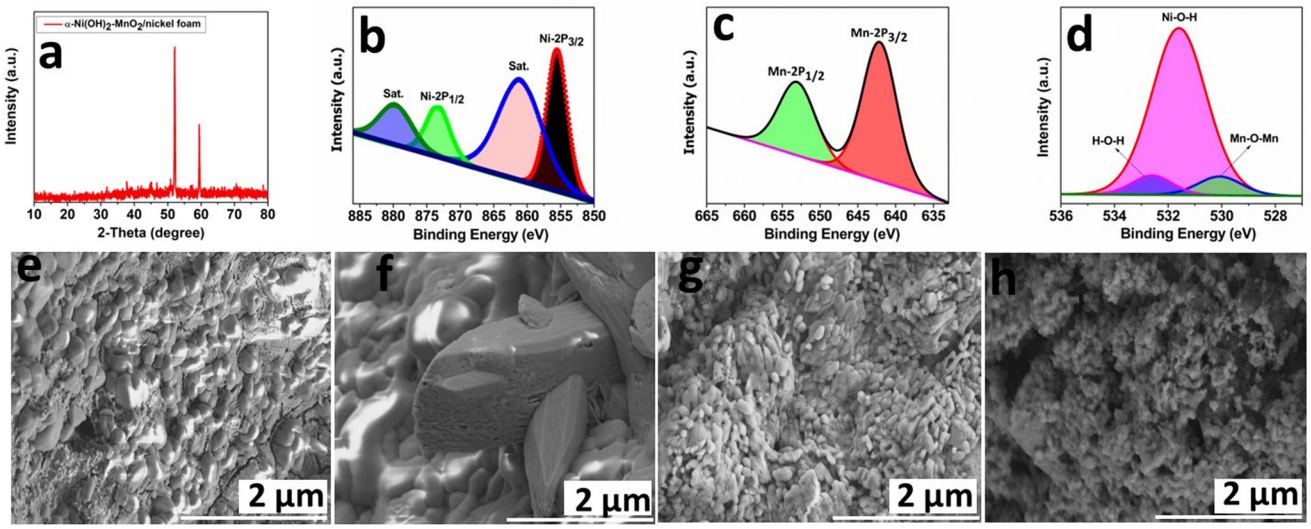

Fig. 8 Top row: (a) PXRD spectrum of α-$Ni(OH)_2$–MnO_2 hybrid on nickel foam, XPS spectra of α-$Ni(OH)_2$–MnO_2 hybrid after stability tests, (b) Ni-2p, (c) Mn-1p, (d) O-1s, bottom row: FE-SEM images of (e) α-$Ni(OH)_2$, (f) NiO, (g) MnO_2, and (h) α-$Ni(OH)_2$–MnO_2 hybrid films after cyclic stability tests.

undergone 5000 charge–discharge cycles (Fig. 8(e–h)) and the images reveal that no major changes have occurred in the morphology of the α-$Ni(OH)_2$, NiO, MnO_2 and α-$Ni(OH)_2$–MnO_2 electrodes after completing the electrochemical stability tests, indicating their excellent structural stability. Furthermore, the FE-SEM images demonstrate that the nanoparticle films remain completely intact at the surface of the nickel foam and do not leach out into the alkaline electrolyte solution.

Conclusion

A surfactant free and scalable methodology for the synthesis of spherical nanoparticles of $Ni(OH)_2$, NiO, and $Ni(OH)_2$–MnO_2 hybrid material employing the polar, aprotic solvent, dimethylformamide has been developed. An extension of the methodology to include a surfactant coated metal oxide nanomaterial (MnO_2) has also been presented for comparison and for such use cases as may be required. The $Ni(OH)_2$ is of the α-phase while the NiO and MnO_2 nanomaterials are tetragonal in phase with their geometry being approximately spherical. Of the electrode materials investigated, surfactant free NiO and α-$Ni(OH)_2$–MnO_2 exhibit the highest specific capacitance of 312.42 mAh g^{-1} and 348.61 mAh g^{-1} at a current density of 1 A g^{-1} in three-electrode configuration, respectively. To evaluate electrochemical performance, symmetric devices were fabricated and tested across a wide operating potential window of 1 V. The NiO and α-$Ni(OH)_2$–MnO_2 based symmetric devices delivered maximum specific capacities of 94.31 mAh g^{-1} and 139.43 mAh g^{-1} at a current density of 1 A g^{-1} and 47.21 Wh kg^{-1} and 69.72 Wh kg^{-1} at a power density of 1 kW kg^{-1} respectively, clearly demonstrating the high-rate capability of the symmetric devices. Devices based on NiO and α-$Ni(OH)_2$–MnO_2 also possess a high cycle stability with maximum

capacity retentions of 86.50% and 90.18% respectively after 5000 charge–discharge cycles at 3 A g^{-1}. These results have clearly demonstrated that this newly developed synthetic protocol is a powerful tool for the fabrication of a range of high quality, crystalline, nanostructured oxidic materials for utilization in electrochemical capacitor applications. Indeed, it is envisaged that this protocol could be employed as the basis to synthesize a range of efficient materials for applications that involve charge transfer processes due to the surfactant free nature of the surfaces.

Conflicts of interest

There are no conflicts of interest to declare.

Data availability

The authors confirm that the data that support the findings of this study are available in the article and its supplementary information (SI). Supplementary information is available. See DOI: https://doi.org/10.1039/d5nr01871d.

All relevant data generated or analyzed during this study are included in this published article and its Supplementary Information. Additional raw data files, are available from the corresponding author upon reasonable request.

Acknowledgements

MNH gratefully acknowledges the Commonwealth Scholarship Commission (CSC) for financial support through the Split-Site programme (PKCN-2019-175). SH acknowledges financial support through the UKIERI-DST Partnership (IND/CONT/G/17-18/36). The authors would like to thank Prof. D. J. Riley for careful reading of the manuscript and subsequent fruitful discussions.

References

1 A. S. Aricò, P. Bruce, B. Scrosati, J.-M. Tarascon and W. Van Schalkwijk, *Nat. Mater.*, 2005, **4**, 366–377.
2 P. Simon and Y. Gogotsi, *Nat. Mater.*, 2008, **7**, 845–854.
3 G. Wang, L. Zhang and J. Zhang, *Chem. Soc. Rev.*, 2012, **41**, 797–828.
4 Y. Hou, Y. Cheng, T. Hobson and J. Liu, *Nano Lett.*, 2010, **10**, 2727–2733.
5 A. L. M. Reddy, M. M. Shaijumon, S. R. Gowda and P. M. Ajayan, *Nano Lett.*, 2009, **9**, 1002–1006.
6 L. L. Zhang and X. S. Zhao, *Chem. Soc. Rev.*, 2009, **38**, 2520.
7 H. Jiang, T. Zhao, C. Li and J. Ma, *J. Mater. Chem.*, 2011, **21**, 3818.
8 R. Zhang, Q. Tu, X. Li, X. Sun, X. Liu and L. Chen, *Nanomaterials*, 2022, **12**, 2216.
9 T. Sichumsaeng, N. Chanlek and S. Maensiri, *Appl. Surf. Sci.*, 2018, **446**, 177–186.
10 X. Liu, Y. Yang, X. Xing, T. Zou, Z. Wang and Y. Wang, *ChemElectroChem*, 2018, **5**, 434–444.
11 N. A. Mala, M. A. Dar, M. U. D. Rather, S. Sivakumar, S. Husain and K. M. Batoo, *Inorg. Chem. Commun.*, 2022, **142**, 109661.
12 M. Mustaqeem, G. A. Naikoo, M. Yarmohammadi, M. Z. Pedram, H. Pourfarzad, R. A. Dar, S. A. Taha, I. U. Hassan, Md. Y. Bhat and Y.-F. Chen, *J. Energy Storage*, 2022, **55**, 105419.
13 X. Liu and F. Liu, *Eur. J. Inorg. Chem.*, 2018, **2018**, 987–991.
14 R. S. Kate, S. A. Khalate and R. J. Deokate, *J. Alloys Compd.*, 2018, **734**, 89–111.
15 O. C. Pore, A. V. Fulari, N. B. Velhal, V. G. Parale, H. H. Park, R. V. Shejwal, V. J. Fulari and G. M. Lohar, *Mater. Sci. Semicond. Process.*, 2021, **134**, 105980.
16 T. Munawar, M. Shahid Nadeem, F. Mukhtar, S. Manzoor, M. Naeem Ashiq and F. Iqbal, *Mater. Sci. Eng., B*, 2022, **284**, 115900.
17 M. N. Hussain, A. Naveed, M. Sohail, M. D. Khan, S. G. Hickey, N. Ullah, I. Ahmad, A. Haider and S. M. Shah, *ACS Appl. Eng. Mater.*, 2025, **3**, 1315–1326.
18 I. Kovalenko, D. G. Bucknall and G. Yushin, *Adv. Funct. Mater.*, 2010, **20**, 3979–3986.
19 H. Wang, H. S. Casalongue, Y. Liang and H. Dai, *J. Am. Chem. Soc.*, 2010, **132**, 7472–7477.
20 W. Wei, X. Cui, W. Chen and D. G. Ivey, *J. Phys. Chem. C*, 2008, **112**, 15075–15083.
21 H. Jiang, C. Li, T. Sun and J. Ma, *Chem. Commun.*, 2012, **48**, 2606.
22 F. Mahdi, M. Javanbakht and S. Shahrokhian, *J. Alloys Compd.*, 2021, **887**, 161376.
23 A. Gowrisankar and T. Selvaraju, *Langmuir*, 2021, **37**, 5964–5978.
24 J. Wu, F. Huang, T. Lee, Y. Yan, X. Pei, M. Wang, S. Gao, S. Guo, X. Pan and P. Wang, *ACS Appl. Energy Mater.*, 2022, **5**, 6962–6969.
25 Y. Zhao, Q. Fang, X. Zhu, L. Xue, M. Ni, C. Qiu, H. Huang, S. Sun, S. Li and H. Xia, *J. Mater. Chem. A*, 2020, **8**, 8969–8978.
26 J. Zhao, B. Zhu, G. Yang, Y. Fu, Y. Lin and J. Li, *J. Phys. Chem. Solids*, 2021, **150**, 109856.
27 Y. Chen, C. Zhou, G. Liu, C. Kang, L. Ma and Q. Liu, *J. Mater. Chem. A*, 2021, **9**, 2872–2887.
28 Z.-H. Huang, Y. Song, D.-Y. Feng, Z. Sun, X. Sun and X.-X. Liu, *ACS Nano*, 2018, **12**, 3557–3567.
29 C. Wei, J. Sun, Y. Zhang, Y. Liu, Z. Guo, W. Du, L. Liu and Y. Zhang, *Inorg. Chem. Front.*, 2022, **9**, 3542–3551.
30 J. Li, C. Wei, Y. Sun, Q. Liu, X. Zhang and J. Guo, *Adv. Mater. Interfaces*, 2019, **6**, 1801470.
31 R. Moreno-Tost, J. Santamaría-González, P. Maireles-Torres, E. Rodríguez-Castellón and A. Jiménez-López, *J. Mater. Chem.*, 2002, **12**, 3331–3336.
32 Y. Wang, Q. Zhu and H. Zhang, *Chem. Commun.*, 2005, 5231.
33 D. Wang, C. Song, Z. Hu and X. Fu, *J. Phys. Chem. B*, 2005, **109**, 1125–1129.

34 B.-H. Liu, S.-H. Yu, S.-F. Chen and C.-Y. Wu, *J. Phys. Chem. B*, 2006, **110**, 4039–4046.
35 J. Q. Qi, T. Zhang, M. Lu, Y. Wang, W. P. Chen, L. T. Li and H. L. W. Chan, *Chem. Lett.*, 2005, **34**, 180–181.
36 M. Cao, X. He, J. Chen and C. Hu, *Cryst. Growth Des.*, 2007, **7**, 170–174.
37 J. Liu, S. Du, L. Wei, H. Liu, Y. Tian and Y. Chen, *Mater. Lett.*, 2006, **60**, 3601–3604.
38 K. Matsui, T. Kyotani and A. Tomita, *Adv. Mater.*, 2002, **14**, 1216–1219.
39 F. Cai, G. Zhang, J. Chen, X. Gou, H. Liu and S. Dou, *Angew. Chem.*, 2004, **116**, 4308–4312.
40 N. D. Hoa and S. A. El-Safty, *Chem. – Eur. J.*, 2011, **17**, 12896–12901.
41 C. Li and S. Liu, *J. Nanomater.*, 2012, **2012**, 648012.
42 X. Zhang, P. Yu, H. Zhang, D. Zhang, X. Sun and Y. Ma, *Electrochim. Acta*, 2013, **89**, 523–529.
43 Y. Tang, Z. Jia, Y. Jiang, L. Li and J. Wang, *Nanotechnology*, 2006, **17**, 5686–5690.
44 L. Dong, Y. Chu and W. Sun, *Chem. – Eur. J.*, 2008, **14**, 5064–5072.
45 H. Jiang, L. Yang, C. Li, C. Yan, P. S. Lee and J. Ma, *Energy Environ. Sci.*, 2011, **4**, 1813.
46 R. Liu and S. B. Lee, *J. Am. Chem. Soc.*, 2008, **130**, 2942–2943.
47 W. Wei, X. Cui, W. Chen and D. G. Ivey, *Chem. Soc. Rev.*, 2011, **40**, 1697–1721.
48 F. Israr, D. Chun, Y. Kim and D. K. Kim, *Ultrason. Sonochem.*, 2016, **31**, 93–101.
49 I. Pastoriza-Santos and L. M. Liz-Marzán, *Adv. Funct. Mater.*, 2009, **19**, 679–688.
50 T. Nagata, K. Okada, R. Kondo, T. Toyao, K. Shimizu, T. Suzuki and Y. Obora, *RSC Adv.*, 2022, **12**, 16599–16603.
51 T. Nagata and Y. Obora, *ACS Omega*, 2020, **5**, 98–103.
52 *Colloidal Synthesis of Plasmonic Nanometals*, ed. L. M. Liz-Marzán, Jenny Stanford Publishing, Singapore, 2020.
53 G. Ramakrishna and H. N. Ghosh, *Langmuir*, 2003, **19**, 505–508.
54 A. Bahaa, J. Balamurugan, N. H. Kim and J. H. Lee, *J. Mater. Chem. A*, 2019, **7**, 8620–8632.
55 H. Liang, C. Xia, Q. Jiang, A. N. Gandi, U. Schwingenschlögl and H. N. Alshareef, *Nano Energy*, 2017, **35**, 331–340.
56 J. Chen, J. Xu, S. Zhou, N. Zhao and C.-P. Wong, *Nano Energy*, 2016, **21**, 145–153.
57 H. Chen, L. Hu, Y. Yan, R. Che, M. Chen and L. Wu, *Adv. Energy Mater.*, 2013, **3**, 1636–1646.
58 G. Zhu, Z. He, J. Chen, J. Zhao, X. Feng, Y. Ma, Q. Fan, L. Wang and W. Huang, *Nanoscale*, 2014, **6**, 1079–1085.
59 M. Shao, F. Ning, J. Zhao, M. Wei, D. G. Evans and X. Duan, *Adv. Funct. Mater.*, 2013, **23**, 3513–3518.
60 M. D. Khan, J. Akhtar, M. A. Malik, M. Akhtar and N. Revaprasadu, *New J. Chem.*, 2015, **39**, 9569–9574.
61 A. Bashir, A. Inayat, R. Bashir, S. Jamil, S. M. Abbas, M. Sultan, A. Iqbal and Z. Akhter, *New J. Chem.*, 2023, **47**, 3560–3571.
62 D. Chao, C. Zhu, P. Yang, X. Xia, J. Liu, J. Wang, X. Fan, S. V. Savilov, J. Lin, H. J. Fan and Z. X. Shen, *Nat. Commun.*, 2016, **7**, 12122.
63 D. Wang, W. Ni, H. Pang, Q. Lu, Z. Huang and J. Zhao, *Electrochim. Acta*, 2010, **55**, 6830–6835.
64 C. Masarapu, H. F. Zeng, K. H. Hung and B. Wei, *ACS Nano*, 2009, **3**, 2199–2206.
65 J. W. Choi, J. McDonough, S. Jeong, J. S. Yoo, C. K. Chan and Y. Cui, *Nano Lett.*, 2010, **10**, 1409–1413.
66 Z. Chen, V. Augustyn, J. Wen, Y. Zhang, M. Shen, B. Dunn and Y. Lu, *Adv. Mater.*, 2011, **23**, 791–795.
67 C.-Y. Cao, W. Guo, Z.-M. Cui, W.-G. Song and W. Cai, *J. Mater. Chem.*, 2011, **21**, 3204.
68 W. G. Nunes, B. G. A. Freitas, R. M. Beraldo, R. M. Filho, L. M. Da Silva and H. Zanin, *Sci. Rep.*, 2020, **10**, 19195.
69 C. Zhou, Y. Zhang, Y. Li and J. Liu, *Nano Lett.*, 2013, **13**, 2078–2085.
70 N. Parveen, *J. Energy Storage*, 2023, **68**, 107762.
71 Z. Li, C. Shi, J. Yu and L. Bai, *Appl. Surf. Sci.*, 2024, **669**, 160534.
72 M. Bulla, V. Kumar, R. Devi, S. Kumar, A. K. Sisodiya, R. Dahiya and A. K. Mishra, *Sci. Rep.*, 2024, **14**, 7389.
73 L. M. Jose, N. S. George, S. A. Kadam, D. A. Nayana and A. Aravind, *Inorg. Chem. Commun.*, 2025, **178**, 114527.
74 O. P. Nanda, S. Chahal and S. Badhulika, *Mater. Chem. Phys.*, 2025, **338**, 130627.
75 R. S. Ingole, S. L. Kadam, R. Kamat, J. G. Ok and S. B. Kulkarni, *Surf. Interfaces*, 2024, **52**, 104976.
76 Q. Ma, W. Hu, D. Peng, R. Shen, X. Xia, H. Chen, Y. Chen and H. Liu, *J. Alloys Compd.*, 2019, **803**, 866–874.